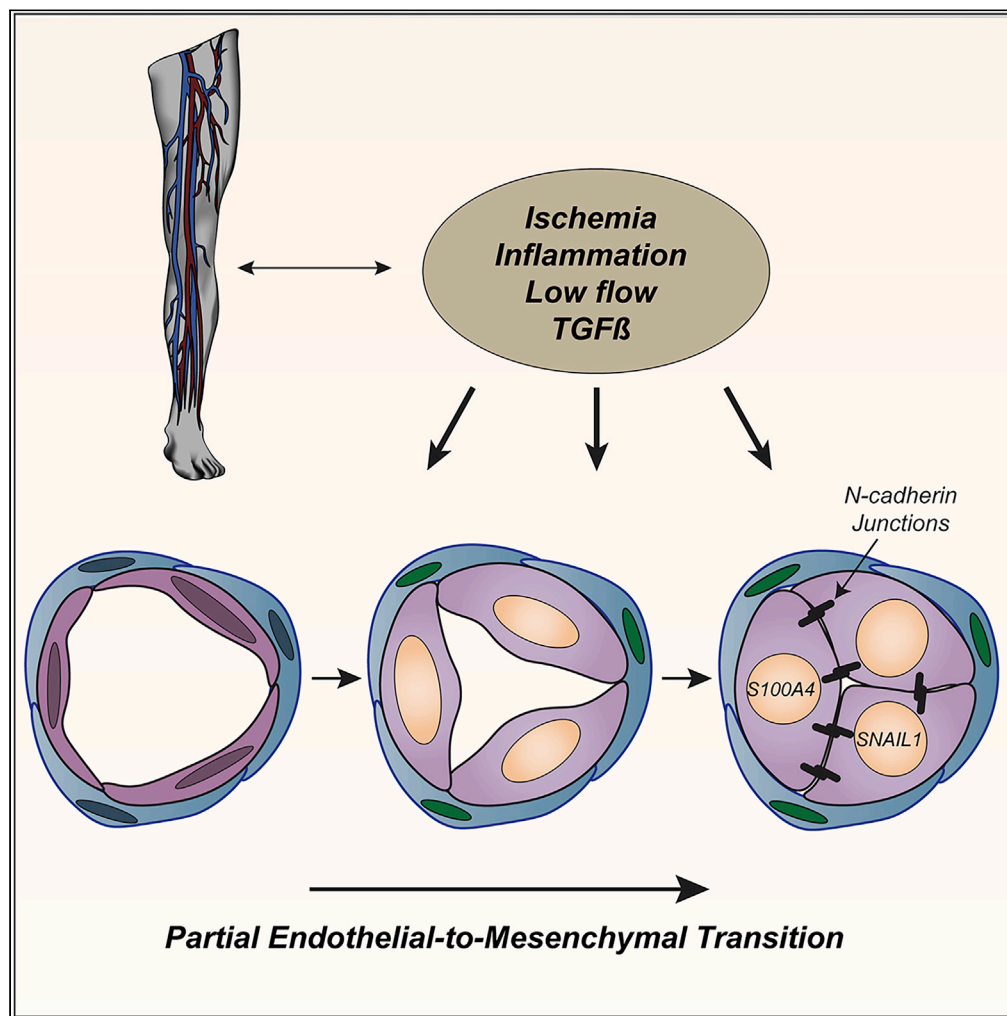


Article

# Obstruction of Small Arterioles in Patients with Critical Limb Ischemia due to Partial Endothelial-to-Mesenchymal Transition



Jacqueline Chevalier, Hao Yin, John-Michael Arpino, ..., Adam H. Power, Douglas W. Hamilton, J. Geoffrey Pickering

gpickering@roberts.ca

**HIGHLIGHTS**

Small arterioles in patients with critical limb ischemia can be narrowed or closed

Arteriolar occlusion is due to bulky endothelial cells

Bulky endothelial cells have partially transitioned to mesenchymal cells

Occlusive cells interlock laterally and apically via N-cadherin neoadhesions

Chevalier et al., iScience 23, 101251  
June 26, 2020 © 2020 The Authors.  
<https://doi.org/10.1016/j.isci.2020.101251>



## Article

## Obstruction of Small Arterioles in Patients with Critical Limb Ischemia due to Partial Endothelial-to-Mesenchymal Transition

Jacqueline Chevalier,<sup>1,3</sup> Hao Yin,<sup>1</sup> John-Michael Arpino,<sup>1,3</sup> Caroline O'Neil,<sup>1</sup> Zengxuan Nong,<sup>1</sup> Kevin J. Gilmore,<sup>6,7</sup> Jason J. Lee,<sup>1,2,3</sup> Emma Prescott,<sup>1,3</sup> Matthew Hewak,<sup>6</sup> Charles L. Rice,<sup>6,7</sup> Luc Dubois,<sup>5</sup> Adam H. Power,<sup>5</sup> Douglas W. Hamilton,<sup>6</sup> and J. Geoffrey Pickering<sup>1,2,3,4,8,\*</sup>

## SUMMARY

**Critical limb ischemia (CLI) is a hazardous manifestation of atherosclerosis and treatment failure is common. Abnormalities in the arterioles might underlie this failure but the cellular pathobiology of microvessels in CLI is poorly understood. We analyzed 349 intramuscular arterioles in lower limb specimens from individuals with and without CLI. Arteriolar densities were 1.8-fold higher in CLI muscles. However, 33% of small (<20 μm) arterioles were stenotic and 9% were completely occluded. The lumens were closed by bulky, re-oriented endothelial cells expressing abundant N-cadherin that uniquely localized between adjacent and opposing endothelial cells. S100A4 and SNAIL1 were also expressed, supporting an endothelial-to-mesenchymal transition. SMAD2/3 was activated in occlusive endothelial cells and TGFβ1 was increased in the adjacent mural cells. These findings identify a microvascular closure process based on mesenchymal transitions in a hyper-TGFβ environment that may, in part, explain the limited success of peripheral artery revascularization procedures.**

## INTRODUCTION

Critical limb ischemia (CLI) is a severe manifestation of atherosclerotic peripheral artery disease (PAD) that produces intractable lower limb pain, non-healing ulcers, and tissue necrosis (Annex, 2013; Shishehbor et al., 2016). To manage advanced PAD and CLI, surgical and catheter-based revascularization procedures are important and widely employed. Unfortunately, however, interventional success may not translate to clinical improvement (Farber and Eberhardt, 2016; Norgren et al., 2007). Moreover, even with early clinical success, long-term failure with recurrent leg ischemia is common. Up to approximately one-third of patients with CLI who have undergone an intervention still require leg amputation within three years (Almasri et al., 2019).

One reason for this burden of refractory PAD may be pathological processes beyond the atherosclerotic narrowing of the large- and medium-sized feeder arteries. Important in this regard is the state of the microvasculature. Microvascular dysfunction in PAD is increasingly appreciated, with evidence for impaired small artery vasoreactivity (Arpino et al., 2017; Coats and Hillier, 2000; Hillier et al., 1999), decreased nitric oxide signaling (Allen et al., 2009; Coats and Hillier, 2000; Hillier et al., 1999), and increased endothelin receptors (Tsui et al., 2002). A modest decrease in skeletal muscle capillary density has also been reported (Clyne et al., 1985; Robbins et al., 2011), although other studies have identified increased capillaries, possibly reflecting an angiogenic response (Hammarsten et al., 1980; Ho et al., 2006; McGuigan et al., 2001; Tsui et al., 2002).

However, the extent to which the reported abnormalities in microvascular vasoreactivity or capillary content can drive CLI, or are the cause of failed revascularization, is uncertain. Importantly, much about the microvasculature in advanced human PAD remains unknown. This includes the fundamental structure of the intramuscular arterioles, a critical component of the arterial tree that controls flow into the capillary bed. Normal arterioles have a relatively simple wall structure, consisting of an endothelial cell monolayer and one or two layers of circumferentially aligned smooth muscle cells (SMCs). However, the small caliber of these pre-capillary vessels makes interrogation of any cellular or morphometric changes in human disease settings challenging. Whether the lumen or wall configuration of small intramuscular arterioles is altered in patients with CLI is unknown.

<sup>1</sup>Robarts Research Institute, Schulich School of Medicine and Dentistry, Western University, London, Canada

<sup>2</sup>Department of Medicine, Schulich School of Medicine and Dentistry, Western University, London, Canada

<sup>3</sup>Department of Medical Biophysics, Schulich School of Medicine and Dentistry, Western University, London, Canada

<sup>4</sup>Department of Biochemistry, Schulich School of Medicine and Dentistry, Western University, London, Canada

<sup>5</sup>Department of Surgery, Schulich School of Medicine and Dentistry, Western University, London, Canada

<sup>6</sup>Department of Anatomy and Cell Biology, Schulich School of Medicine and Dentistry, Western University, London, Canada

<sup>7</sup>School of Kinesiology, Faculty of Health Sciences, Western University, London, Canada

<sup>8</sup>Lead Contact

\*Correspondence: [gpickering@robarts.ca](mailto:gpickering@robarts.ca)  
<https://doi.org/10.1016/j.isci.2020.101251>



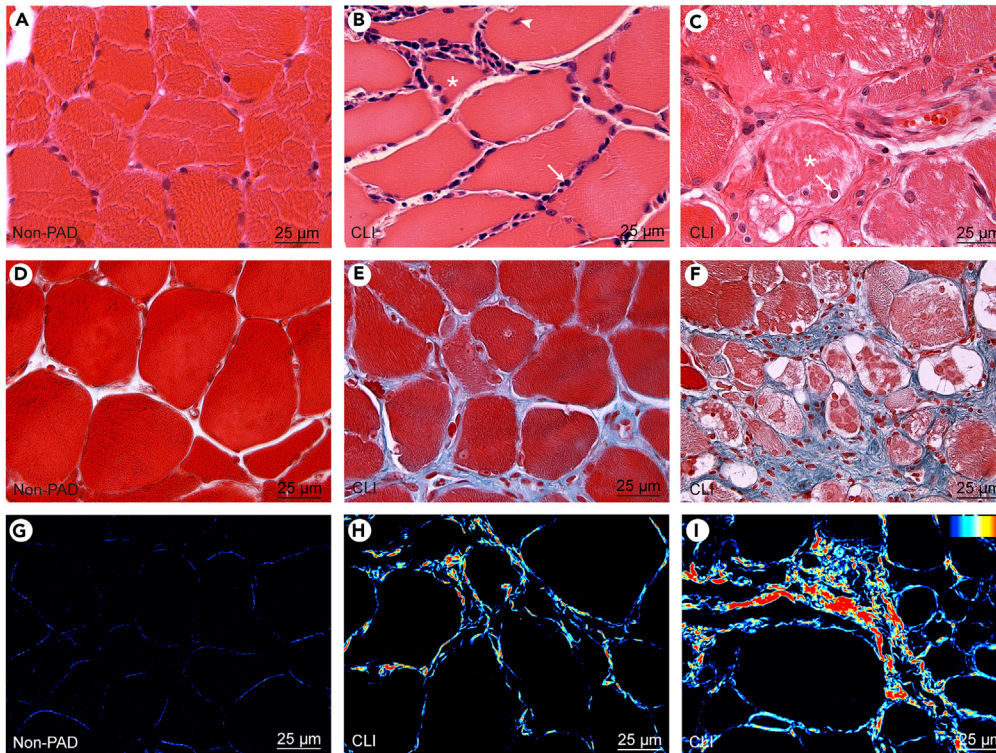


**Figure 1. Histopathology of Human Skeletal Muscle in Patients with CLI**

(A–C) H&E-stained sections of non-PAD muscle (A) and CLI muscles (B and C). CLI muscle features include a triangular, shrunken myofiber (asterisk, B), interstitial inflammation (arrow, B), a myofiber with an internal nucleus (arrowhead, B), myofiber degeneration and necrosis (asterisk, C), and intra-myofiber inflammatory cell infiltration (arrow, C). (D–F) Mason's-trichrome-stained sections of non-PAD muscle (D) and CLI muscles (E and F), the latter showing interstitial accumulation of collagen-containing extracellular matrix (E) and myofibers replaced by collagen (F). (G–I) Images of picosirius red-stained sections of non-PAD muscle (G) and CLI muscles (H and I) imaged with circularly polarized light and color mapped based on light retardation. Thin, weakly birefringent collagen fibrils can be seen surrounding non-PAD myofibers (G). CLI muscles display accumulation of interstitial collagen fibrils (H) and regions of scarring with replacement fibrosis (I). The light retardation color map is shown, and all images are captured and level adjusted with identical settings.

See also [Figure S1](#) and [Table S2](#).

Herein, we report the phenomenon of non-atherosclerotic, non-thrombotic narrowing of small arterioles in the lower limb muscle of individuals with CLI. We also report that the luminal narrowing of these distal arterioles is based on partial endothelial-to-mesenchymal transition (EndMT). The findings uncover a previously unrecognized microvascular closure process that could underlie the debilitating consequences of critical limb ischemia.

## RESULTS

### Clinical Characteristics and Skeletal Muscle Pathology

To elucidate the status of microvessels in the afflicted skeletal muscle of individuals with CLI, we harvested 24 muscle samples from 10 amputated lower limbs. All subjects had a Rutherford category six level of lower limb ischemia. Demographic features including age, smoking, diabetes, and hypertension are depicted in [Table S1](#). Half of the patients had prior revascularization of the subsequently amputated limb. For comparator tissues, lower limb muscle specimens from six individuals without PAD or known risk factors for vascular disease were studied ([Table S1](#)). Mean patient age was not significantly different between the two groups ( $65 \pm 16$  versus  $52 \pm 17$ ,  $p = 0.14$ ).

All 24 CLI muscle samples displayed myofiber atrophy, evidenced by shrunken myofibers with either rounded or sharply angular, typically triangular, borders ([Figure 1](#), [Table S2](#)). This contrasted with the larger, polygonal cross-sectional morphology of myofibers in the non-PAD skeletal muscle. Quantitative assessment revealed a significantly lower mean myofiber area in CLI subjects than in non-PAD subjects ( $p = 0.025$ , [Figure S1](#)). There were no

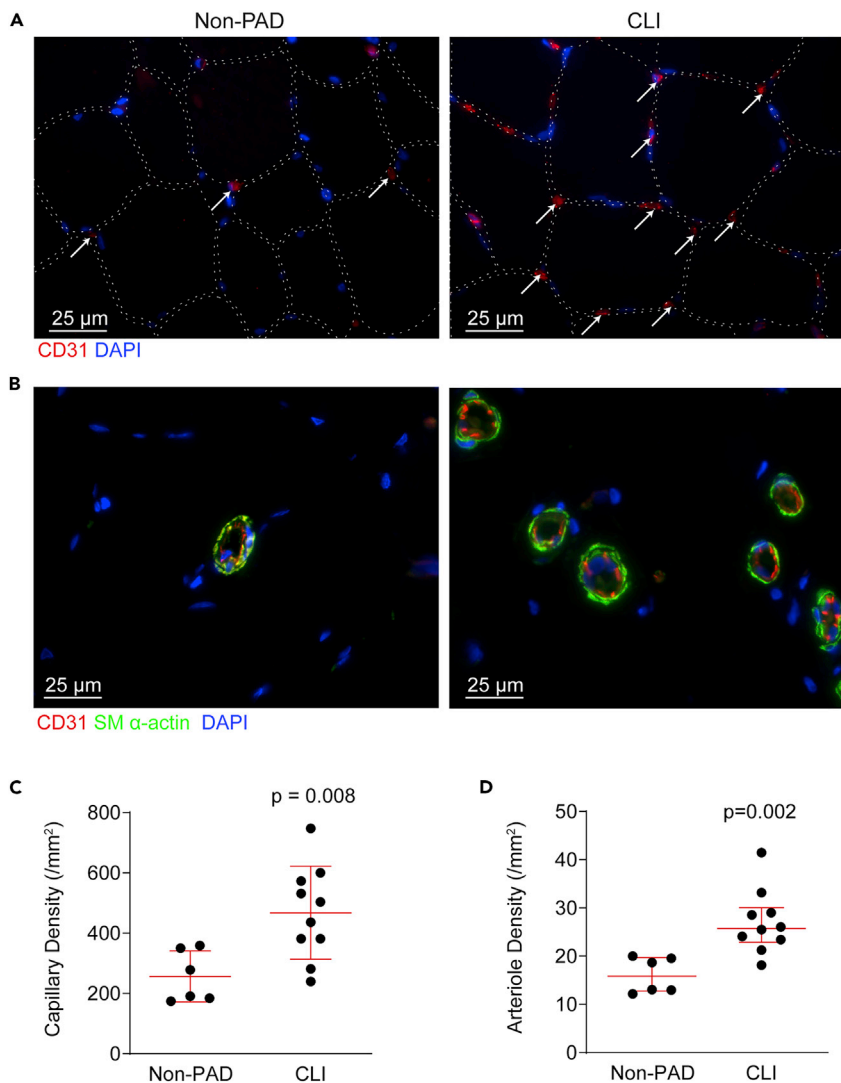


**Figure 2. Capillary and Arteriole Density in Skeletal Muscle of Patients with CLI**

(A) Fluorescence micrographs of human skeletal muscle immunostained for CD31 (red) showing capillaries (arrows) between myofibers (dotted lines) in non-PAD (left) and CLI (right) muscles. Nuclei were counterstained with DAPI (blue). (B) Fluorescence micrographs of human skeletal muscle double immunostained for CD31 (red) and SM  $\alpha$ -actin (green) showing arterioles in non-PAD and CLI muscles. (C) Graph depicting capillary densities in skeletal muscles of non-PAD subjects ( $n = 6$ ) and CLI subjects ( $n = 10$ ). (D) Graph depicting arteriole density in skeletal muscle from non-PAD and CLI subjects. Means  $\pm$  standard deviations are shown.

differences in myofiber area among the different muscles in CLI patients ( $p = 0.51$ , Figure S1). In addition to myofiber atrophy, there was also overt myofiber necrosis in nine of ten CLI patients (18 of 24 muscle samples), and eight patients (16 samples) displayed at least one myofiber with an internal nucleus, suggesting a degree of myocyte regeneration. Inflammatory cell infiltration into the endomysium was evident in nine patients (18 samples) and fibrosis was evident in 8 patients (14 samples). Circular polarization microscopy (Vafaie et al., 2014; Whittaker et al., 1994) established thin collagen fibrils in the endomysium of non-PAD muscle but interstitial and replacement fibrosis with thick collagen fibrils in CLI muscles (Figure 1).

### Capillary and Arteriole Densities Are Increased in CLI Skeletal Muscle

To evaluate the abundance of microvessels in CLI skeletal muscle, sections were double immunostained for endothelial cells and SMCs, using antibodies for CD31 and SM  $\alpha$ -actin, respectively (Figure 2). Capillary

density was 1.8-fold higher in CLI muscles than non-PAD muscles ( $p = 0.008$ , [Figure 2C](#)), suggesting an angiogenic response in the ischemic muscles. Interestingly, arteriolar density (8–60  $\mu\text{m}$  diameter) was also 1.8-fold greater in CLI samples ( $p = 0.002$ , [Figure 2D](#)). Thus, despite the critical ischemia, there was no net loss of muscle microvessels but a modest increase of both capillaries and intramuscular arterioles.

### Arterioles within CLI Muscle Display Luminal Stenosis

We next evaluated the wall structure of the intramuscular arterioles. Interestingly, the cross-sectional morphometry of CD31/SM  $\alpha$ -actin double-immunolabeled arterioles revealed unusual heterogeneity. Some arterioles had the traditional appearance of an open lumen, a flattened endothelial cell layer, and one or two layers of SMCs ([Figure 3](#)). However, other arterioles had lumens that were remarkably narrowed and, in some cases, entirely occluded ([Figure 3](#), [Videos S1](#) and [S2](#)). There was no evidence for thrombus in the narrowed or occluded lumens ([Figures 3](#) and [S2](#)). Instead, the lumens were obstructed by unusually shaped, CD31-positive endothelial cells. These cells were pyramidal or cuboidal in shape, had enlarged nuclei, and they encroached on the lumen ([Figures 3](#) and [S2](#)).

Narrowed or occluded lumens were particularly evident in the smaller arterioles. To quantify this, for each subject we assessed arterioles with an outer endothelial circumference of  $\leq 60 \mu\text{m}$ , corresponding to diameters taken from the outer endothelial surface of  $< \sim 20 \mu\text{m}$ . This entailed a total of 314 and 35 arterioles in CLI and non-PAD subjects, respectively. On a per subject basis, the mean lumen area of CLI arterioles was 28% lower than that in the non-PAD arterioles ( $p = 0.038$ , [Figure 3B](#)). The lumen area of the small arterioles did not differ among muscle groups ( $p = 0.96$ , [Figure S3](#)). Importantly, the reduced lumen area in arterioles of CLI versus non-PAD subjects persisted when accounting for arteriolar size, across a range of 20–60  $\mu\text{m}$  in circumference ( $p < 0.0001$ , [Figure 3C](#)).

The endothelial cell basis for the luminal narrowing was also confirmed quantitatively. Specifically, the fractional endothelial cell area, defined as the endothelial cell area divided by the total area bounded by the outer endothelial cell border, was on average 19% greater in CLI arterioles than in non-PAD arterioles ( $p = 0.0005$ , [Figure 3D](#)). To assess the prevalence of endothelial-cell-based stenosis in CLI arterioles, we ascertained a 90% prediction band for normal fractional endothelial cell area, based on values for the non-PAD arterioles. Based on the upper threshold, this revealed that 33% of CLI small arterioles had narrowed lumens and 9% were entirely occluded ([Figure S4](#)). The observed shape change and re-orientation of endothelial cells in CLI arterioles corresponded to nuclear shape changes, which we quantitatively assessed by measuring the nuclear aspect ratio (width-to-height, i.e. the orthogonal circumferential and radial dimensions). In non-PAD arterioles, this ratio was 2.2, whereas in CLI arterioles it was 1.5 ( $p < 0.006$ , [Figure 3E](#)).

### Obstructive Endothelial Cells Display Abundant N-cadherin, Atypically Located at Cell-Cell Junctions

Given the morphological shift away from a classically flattened endothelial cell, we asked if the endothelial cells in CLI arterioles had acquired attributes of mesenchymal cells. We were particularly interested in cell-cell adhesion components, recognizing the substantially expanded interface between adjacent endothelial cells in CLI arterioles. N-cadherin is abundant in mesenchymal cells where it localizes to intercellular homotypic adherens junctions. However, in normal microvascular endothelial cells, N-cadherin is a minor, diffusively expressed cadherin with a role in endothelial cell-mural cell anchorage ([Gerhardt et al., 2000](#); [Gilbertson-Beadling and Fisher, 1993](#); [Navarro et al., 1998](#)). Upon double-immunolabeling for CD31 and N-cadherin, we observed weak, diffuse N-cadherin signals in endothelial cells of non-PAD arterioles ([Figure 4A](#)), consistent with previous reports ([Navarro et al., 1998](#)). However, in endothelial cells of CLI arterioles the N-cadherin signal was more intense, with mean N-cadherin content being 2.4-fold greater than on endothelial cells of non-PAD arterioles ( $p = 0.0004$ , [Figure 4B](#)). We also compared the endothelial N-cadherin expression, in a given CLI section, between arterioles that were fully open versus those that were narrowed or fully occluded, pooling the latter two categories given the relatively small number of fully occluded arterioles. This revealed that N-cadherin abundance in endothelial cells of arterioles with a narrowed or occluded lumen was, on average, 32% higher than that in endothelial cells lining arterioles with an open lumen ( $p = 0.0003$ , [Figure 4C](#)). Also striking was that in narrowed or occluded CLI arterioles, N-cadherin concentrated and localized at the interface between endothelial cells. This was evident at the lateral interface between adjacent endothelial cells and also at the apical interface of two opposing and contacting endothelial cells in occluded lumens ([Figure 4A](#)). Intriguingly, apical endothelial cell N-cadherin complexes were also found in arterioles in which endothelial cells protruded into the lumen but without fully contacting the opposing endothelial cell ([Figure 4A](#), [Video S3](#)).

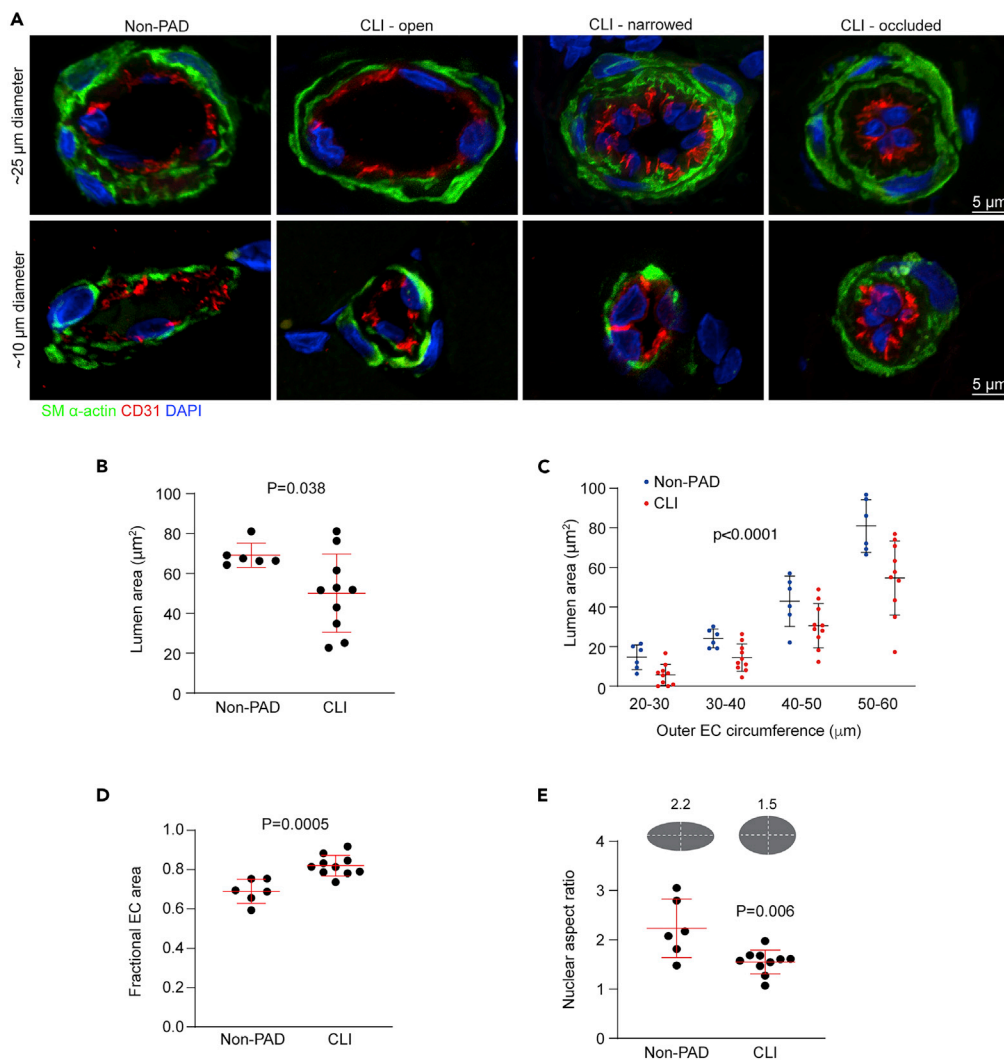


### Figure 3. Arteriolar Lumen and Endothelial Cell Morphometry in CLI Muscles

(A) Confocal microscope images of pre-terminal (~25 μm diameter) and terminal (~10 μm) arterioles in human skeletal muscle immunostained for CD31 (red) and SM α-actin (green). Nuclei were counterstained with DAPI (blue). The lumen of CLI arterioles can be open with a flattened endothelial monolayer, narrowed by thickened and re-oriented endothelial cells, or entirely occluded by swollen endothelial cells with bulky nuclei.

(B) Lumen area of small arterioles (circumference at the outer endothelial cell border <60 μm) from CLI subjects (n = 10, total 314 arterioles measured) and non-PAD subjects (n = 6, total 35 arterioles). Lumen areas are averaged per subject. (C) Mean lumen area of small arterioles from CLI and non-PAD subjects binned based on vessel circumference. Overall p < 0.0001; post-hoc p = 0.035, 0.037, 0.226, and 0.038, respectively.

(D) Graph depicting fractional endothelial cell area of arterioles in non-PAD and CLI subjects.

(E) Nuclear aspect ratio (width-to-height) of endothelial cells of small arterioles in non-PAD and CLI subjects. A total of 119 and 1,450 nuclei were measured, respectively, and the data are presented as average per subject. Shapes depict the nuclei with mean aspect ratios. Means ± standard deviations are shown.

See also [Figures S2–S4](#).

### Obstructive Endothelial Cells in CLI Arterioles Have Undergone Partial Endothelial-to-Mesenchymal Transition

The above findings suggested that, although endothelial cell identity persisted, there was a shift toward mesenchymal attributes in the endothelium of CLI arterioles. In an effort to substantiate this, we immunolabeled skeletal muscle sections for the mesenchymal cell marker, S100A4, also known as fibroblast-specific protein. Diffuse S100A4 signal was observed in endothelial cells of some non-PAD arterioles, with 14% of arterioles displaying at least one S100A4-positive endothelial cell. However, there was a 2.2-fold increase in

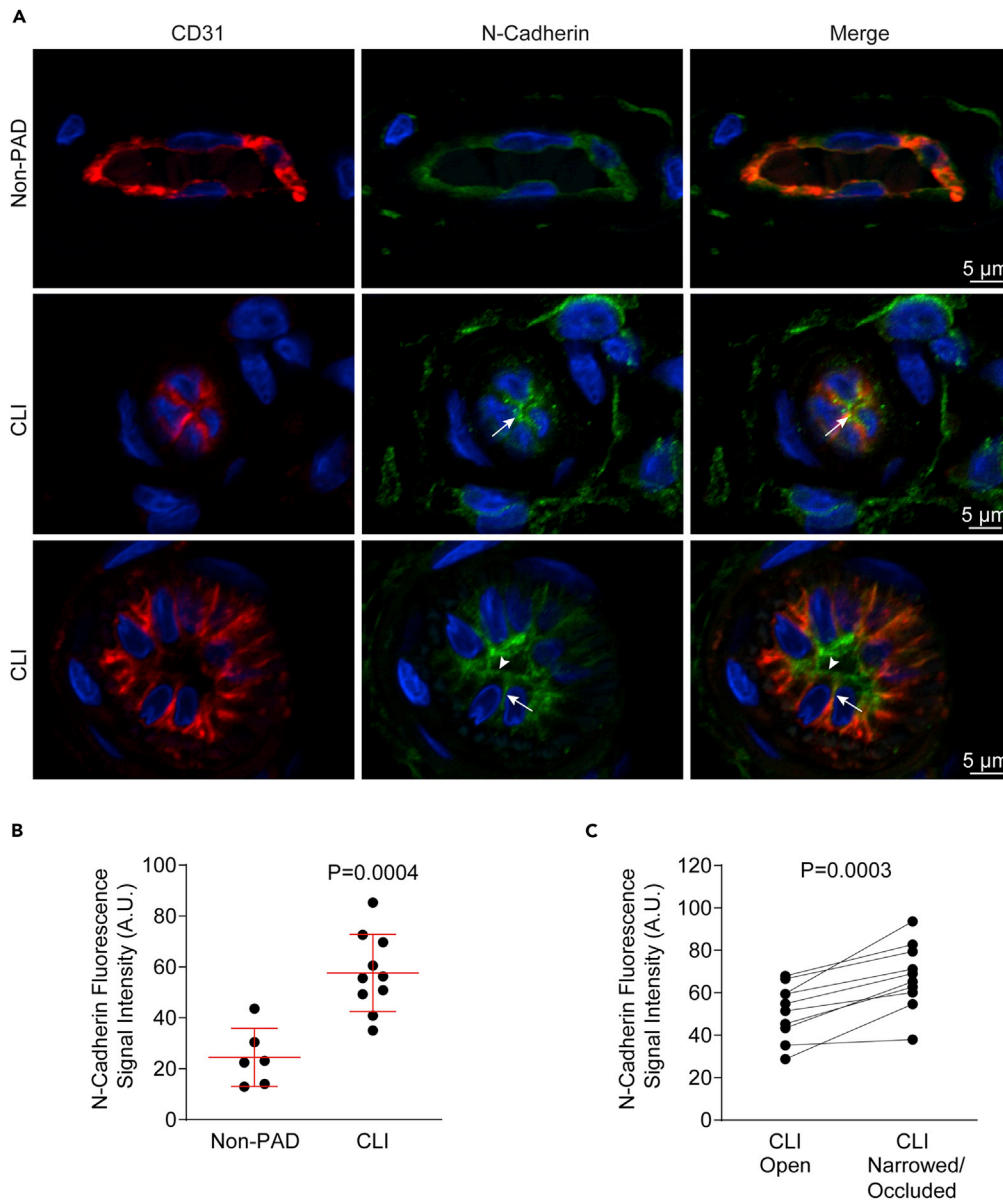


**Figure 4. Reconfigured N-cadherin in Endothelial Cells of Arterioles in CLI Muscle**

(A) Confocal micrographs of human skeletal muscle arterioles immunostained for CD31 (red) and N-cadherin (green), with nuclei counterstained with DAPI (blue). *Top row* shows diffuse endothelial cell N-cadherin signal in a non-PAD arteriole. *Middle row* shows an arteriole that is occluded by bulky, pyramidal-shaped endothelial cells, with enriched N-cadherin signal at junctions between adjacent and opposing endothelial cells (arrows). *Bottom row* shows an arteriole that is substantially narrowed by columnar endothelial cells, with enriched N-cadherin signal between adjacent endothelial cells (arrow) and also at the apical cell surface (arrowhead).

(B) Graph depicting N-cadherin signal intensity in arteriolar endothelium in muscles from non-PAD and CLI patients. Pooled data are represented as mean  $\pm$  standard deviation.

(C) N-cadherin signals in endothelium of CLI arterioles with open lumens and CLI arterioles with narrowed or fully occluded lumens. Data from open-lumen and narrowed/occluded-lumen arterioles from a given patient are denoted by the adjoining lines.

the number of arterioles with S100A4-positive endothelial cells in the CLI muscle muscles ( $p = 0.006$ , [Figures 5A and 5C](#)). In addition, the proportion of narrowed or closed-lumen CLI arterioles with S100A4-positive endothelial cells was 7.4-fold higher than that in open-lumen CLI arterioles ( $p < 0.0001$ , [Figure 5D](#)).

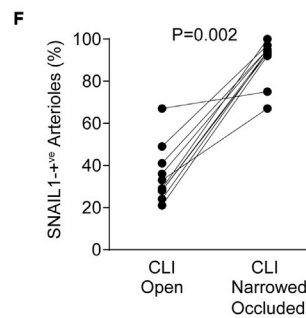
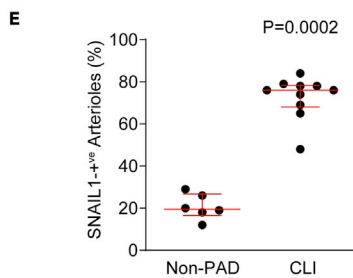
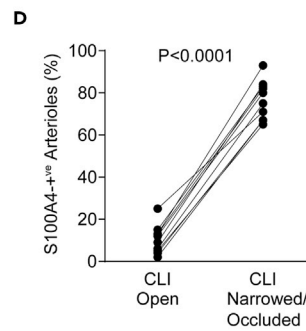
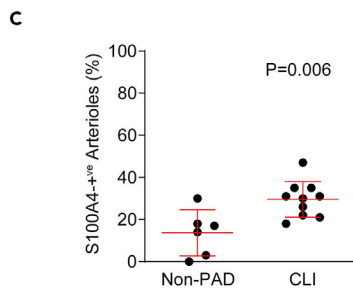
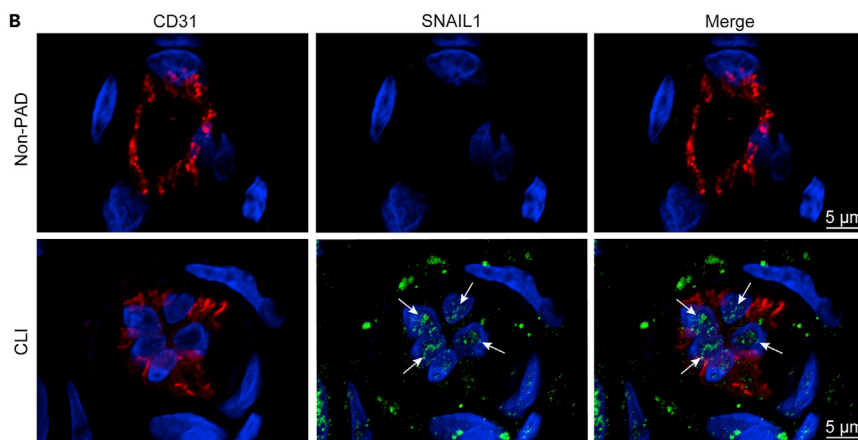
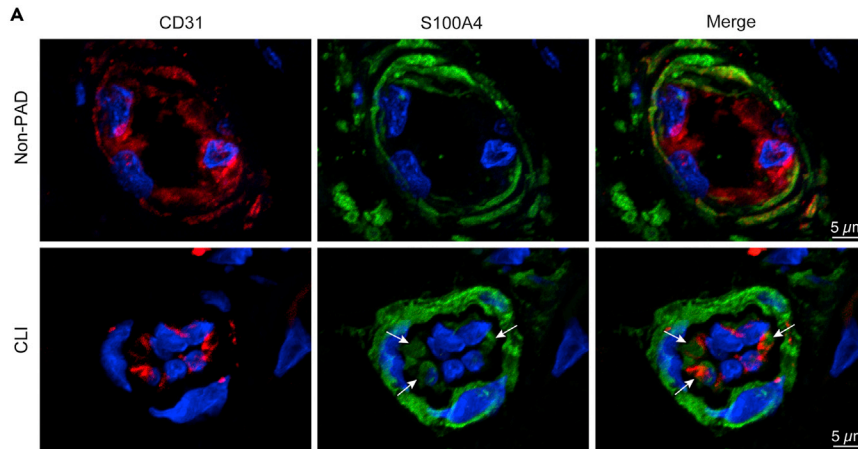


**Figure 5. Mesenchymal Markers S100A4 and SNAIL1 in Endothelial Cells of Stenotic Arterioles in CLI Muscle**

- (A) Confocal micrographs of arterioles in non-PAD and CLI muscle immunostained for CD31 (red) and S100A4 (green), showing cytoplasmic S100A4 signal in endothelial cells of a CLI arteriole with a narrowed lumen (arrow).  
 (B) Confocal micrographs showing punctate SNAIL1 signal (green) in the nuclei of endothelial cells of a CLI arteriole with a narrowed lumen (arrow).  
 (C) Graph depicting the proportion of endothelial S100A4-positive arterioles in muscles from non-PAD and CLI patients (mean  $\pm$  standard deviation).  
 (D) Proportion of endothelial S100A4-positive CLI arterioles with open and narrowed/occluded lumens. Data from open-lumen and narrowed/occluded-lumen arterioles from a given patient are denoted by the adjoining lines.  
 (E) Proportion of SNAIL1-positive endothelial cells in arterioles in non-PAD and CLI muscle samples (median  $\pm$  interquartile range).  
 (F) Proportion of endothelial SNAIL1-positive CLI arterioles with open and narrowed/occluded lumens (F). Data from open-lumen and narrowed/occluded-lumen arterioles from a given patient are denoted by the adjoining lines.

We next assessed for expression of the EndMT-related transcription factor, SNAIL1. There was a low abundance of endothelial SNAIL1 signal in non-PAD arterioles. However, 76% of arterioles within CLI muscles had at least one endothelial cell with punctate, nuclear SNAIL1 signals ( $p = 0.0002$ , Figures 5B and 5E). Within CLI tissues, the proportion of arterioles with SNAIL1-positive endothelial cells was 3.0-fold higher in narrowed or occluded arterioles than in open-lumen CLI arterioles ( $p = 0.002$ , Figure 5F).

Together, these findings strongly suggest that endothelial cells in the small intramuscular arterioles of CLI patients undergo partial EndMT.

**Obstructive Endothelial Cells in CLI Arterioles Receive Increased TGF $\beta$  Signals**

Signaling from TGF $\beta$  is known to increase expression and activity of EndMT transcription factors (Evrard et al., 2016; Kovacic et al., 2019). SMAD2 and SMAD3 become phosphorylated at their carboxy termini following cell stimulation by TGF $\beta$ . Therefore, we immunolabeled skeletal muscle tissues for pSMAD2/3 to ascertain if obstructing endothelial cells in arterioles were receiving TGF $\beta$  signals. A moderate abundance of nuclear, punctate pSMAD2/3 signal was found in endothelial cells of non-PAD arterioles. However, the proportion of arterioles with activated SMAD2/3 signals was 1.4-fold higher in CLI tissue ( $p = 0.030$ , Figures 6A and 6C). As well, endothelial pSMAD2/3 signals were greatest in CLI arterioles with a narrowed or closed lumen (10.9-fold more than in CLI arterioles with open lumens,  $p < 0.0001$ , Figure 6D).

To gauge the potential source of TGF $\beta$  signals, tissues were immunostained for TGF $\beta$ 1. Interestingly, although TGF $\beta$ 1 was barely detectable in non-PAD arterioles, it was relatively abundant in the arterioles of CLI muscle, with a 7.3-fold increase in overall mean signal per arteriole ( $p = 0.0002$ , Figures 6B and 6E). Also interesting was that the increased TGF $\beta$ 1 abundance was a feature primarily of the arteriolar SMCs, not arteriolar endothelial cells (Figure 6B). As well, in CLI muscles, those arterioles with narrowed or closed lumens had higher arteriolar TGF $\beta$  signals than those with open lumens ( $p = 0.014$ , Figure 6F). These findings reveal a state of TGF $\beta$  hyperactivity within arterioles of individuals with CLI, with abundant TGF $\beta$  in the SMCs and pronounced TGF $\beta$  signaling in the adjacent endothelial cells.

**DISCUSSION**

The state of the microvessels may be critical to outcomes in PAD. In this study, we have identified that the lumen of small intramuscular arterioles in patients with CLI can be narrowed, and in some cases completely occluded, by the lining endothelial cells. The culprit endothelial cells were cuboidal, rather than flattened, and displayed molecular attributes of having undergone partial EndMT. This endothelial phenotype shift, and the associated luminal obstruction, constitutes a previously unrecognized arteriolar remodeling process that could exacerbate malperfusion of muscles, and compromise revascularization outcomes, in patients with CLI.

**Arteriolar Obstruction in CLI**

Currently established modes of arteriolar obstruction include vasculitis (Saygin et al., 2019), thrombosis (Springer and Villa-Forte, 2013), and cholesterol emboli (Narula et al., 2018). In CLI, the potential for thromboembolic events has recently been highlighted by finding chronic thrombi in the leg arteries and thrombi in small subcutaneous arteries (Narula et al., 2018). In the current study, we focused further down the vascular tree, specifically on the intramuscular arterioles. Our finding of endothelial-cell-based stenosis was particularly prevalent in arterioles less than 20  $\mu$ m in diameter. In these small arterioles, we found little

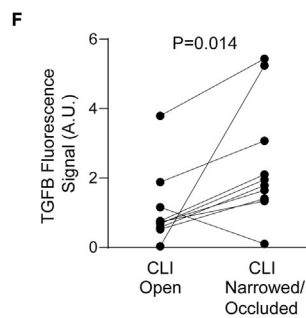
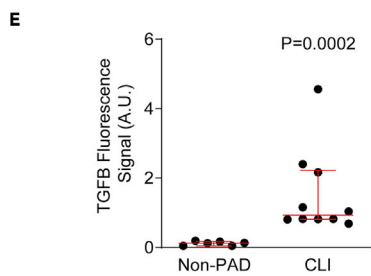
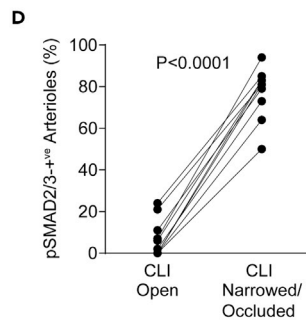
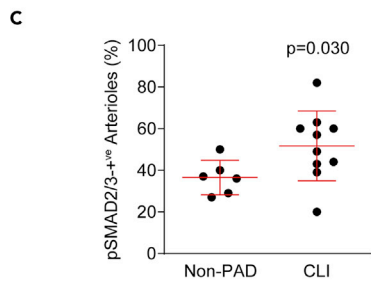
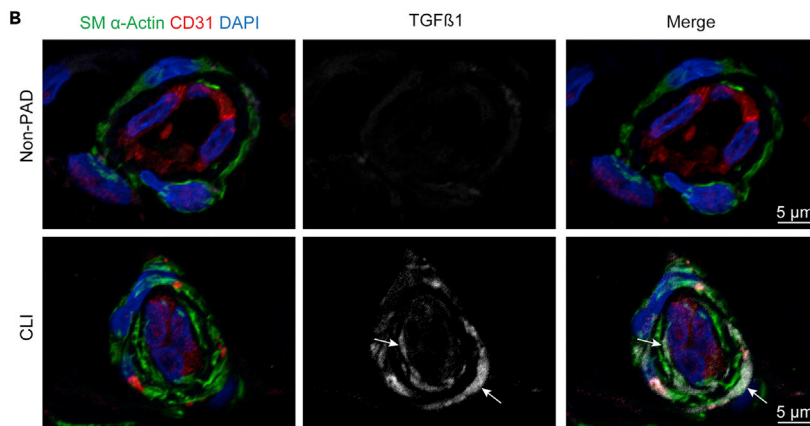
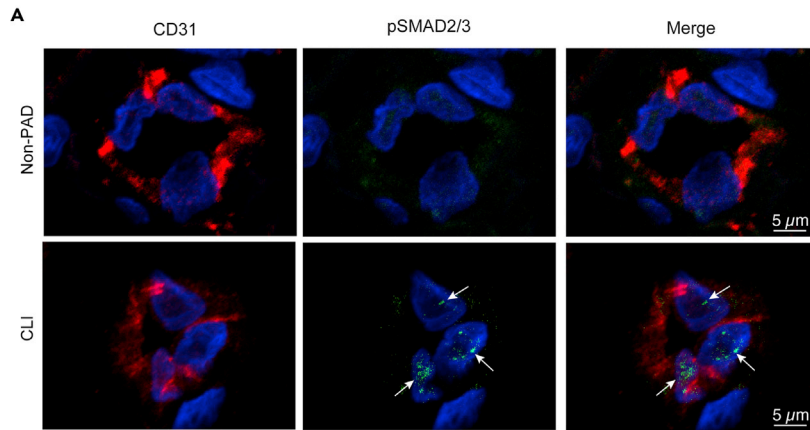


**Figure 6. Hyperactive TGF $\beta$  Signaling in Occluded Arterioles**

- (A) Confocal micrographs of arterioles in non-PAD and CLI muscle immunostained for CD31 (red) and pSMAD2/3 (green) showing discrete punctate signals of phosphorylated SMAD2/3 (pSMAD2/3) in the nucleus of endothelial cells within the CLI arteriole (arrow). Nuclei were counterstained with DAPI (blue).
- (B) Confocal micrographs of arterioles in non-PAD and CLI muscle immunostained for CD31 (red), SM  $\alpha$ -actin (green), and TGF $\beta$ 1 (white). Nuclei were counterstained with DAPI (blue). TGF $\beta$ 1 signal was predominantly observed in SMCs of the CLI arteriole (arrows).
- (C) Proportion of endothelial pSMAD2/3-positive arterioles in muscle samples from non-PAD and CLI subjects (mean  $\pm$  standard deviation).
- (D) Proportion of endothelial pSMAD2/3-positive CLI muscle arterioles with either open or narrowed/occluded lumens.
- (E) Graph depicting TGF $\beta$ 1 content (median  $\pm$  interquartile range) in arterioles in non-PAD and CLI subjects.
- (F) TGF $\beta$ 1 content in skeletal muscle arterioles with either open or narrowed/occluded lumens. For D and F, arteriole data from a given patient are depicted by the adjoining lines. A.U., arbitrary units of integrated fluorescence intensity.

to no evidence for thrombi, cholesterol emboli, or perivascular inflammatory cell infiltration. Instead, the bulky and re-oriented microvascular endothelial cells themselves were the apparent culprits for the lumen narrowing process. Given that 42% of small arterioles showed some luminal narrowing due to bulky endothelial cells, this process has the potential to significantly compromise limb perfusion in this high-risk population. Interestingly, we also found increased densities of capillaries and arterioles in the ischemic muscle samples. We speculate that the potential benefits of this neovascular response could be mitigated by the arteriolar narrowing process we identified.

In hypertension, small resistance arteries can undergo inward remodeling, wherein the lumen diameter decreases and medial thickness increases (Laurent and Boutouyrie, 2015; Park and Schiffrin, 2001). This process has been identified in vessels that are generally 100–300  $\mu$ m in diameter and thus at a higher location in the small vessel tree. Also, this form of remodeling is based on changes in the lumen-to-media ratio, not on endothelial cell remodeling (Feihl et al., 2008). Thus, although we cannot exclude concomitant SMC-based remodeling, the endothelial-cell-based arteriolar narrowing and occlusion we identified in CLI patients appears to be a distinct form of microvascular remodeling. Interestingly, vascular casting studies by Margaret Conrad in the 1960s revealed occlusions in the distal small arterioles in limbs of individuals with CLI (Conrad, 1967, 1968). This included 17% of arterioles below 30  $\mu$ m in the toes and nail beds (Conrad, 1968). Although the basis for these occlusions is not known, it is interesting to speculate that these early findings reflected, at least in part, endothelial-cell-based obstructions.

**Partial EndMT and Arteriolar Obstruction**

The classical paradigm of EndMT entails endothelial cells degrading their basement membrane and sprouting off the vessel wall to become interstitial fibrogenic cells (Dejana et al., 2017; Kovacic et al., 2019). However, evidence is emerging that EndMT can comprise a spectrum, with variability in the phenotype to which the endothelial cell transitions (Kovacic et al., 2019; Nagai et al., 2018; Sanchez-Duffhues et al., 2016). Partial EndMT is the term employed when at least one key characteristic of complete EndMT is not exhibited (Welch-Reardon et al., 2015). In the intramuscular arterioles of CLI patients, the endothelial cells maintained CD31 expression and remained on the luminal side of the vessel. However, despite being toward the “endothelial end” of a spectrum, they were also abnormally bulky and expressed the mesenchymal markers S100A4, SNAIL1, and N-cadherin. Importantly, co-localization of these mesenchymal markers with CD31 in the same cell was validated with high-resolution (X-Y, 0.100  $\mu$ m; Z, 0.125  $\mu$ m) confocal microscope imaging, including 3D reconstructions. This high-resolution approach also confirmed that the rounded occlusive endothelial cells were not trapped leukocytes expressing CD31 (e.g. see Video S2).

Why the transitioned endothelial cells did not progress to a migratory and invasive state is not known but may be related to the specifics of upstream drivers of EndMT in the CLI milieu. In addition, there are SMCs and abundant extracellular matrix within arterioles, which, in contrast to the capillary environment, could constitute barriers to outward endothelial cell translocation. Ultimately, the consequence for CLI arterioles was that mesenchymal-transitioned endothelial cells remained in their native location, where their bulky morphology could compromise lumen patency.

**Reconfigured Endothelial Cell N-cadherin in CLI Arterioles**

It is noteworthy that N-cadherin was not only abundant in CLI arteriolar endothelial cells but also uniquely localized. In small arterioles of non-PAD limbs, the endothelial N-cadherin signal was diffuse, consistent

with previous reports showing dispersed N-cadherin on the endothelial cell membrane (Navarro et al., 1998; Salomon et al., 1992). In contrast, in CLI arterioles, there were discrete N-cadherin signals between adjacent endothelial cells. This striking shift implicates a change in N-cadherin roles. In normal arterioles N-cadherin can be found at the endothelial cell-SMC interface (Isakson et al., 2008), and a role in endothelial cell-pericyte connections has been found in the developing brain (Gerhardt et al., 2000). However, N-cadherin does not typically mediate endothelial cell-endothelial cell interactions, which, instead, is accomplished by VE-cadherin (Navarro et al., 1998). Our finding of N-cadherin at the interface between endothelial cells in CLI arterioles thus implicates cadherin switching (Wheelock et al., 2008) in the ischemic limbs of individuals with PAD.

Finding N-cadherin between opposing endothelial cells in fully occluded arterioles is particularly intriguing. The concentration of N-cadherin between the respective apical surfaces suggests the formation of firm connections that keep the lumen closed. In this regard, it is noteworthy that N-cadherin, a type 1 cadherin, can promote stronger intercellular adhesiveness than type 2 cadherins, of which VE cadherin is a canonical member (Chu et al., 2006). The finding of apical N-cadherin in endothelial cells that were not physically contacting an opposing endothelial cell is also noteworthy. Although we cannot exclude post-harvesting retraction of the endothelial cells, an interesting comparison exists with the developing neural tube, where an evolutionarily conserved phenomenon of apical enrichment of N-cadherin plays a role in neuroepithelial cyto-architecture and neural tube closure (Bronner-Fraser et al., 1992; Rousso et al., 2012). Taken together, we speculate that the emergence of N-cadherin complexes on mesenchymally transitioned endothelial cells allows for more widespread and stronger inter-cellular connections, not just on the lateral edges as for VE cadherin but also on the expanding lateral and apical interfacial surfaces. Further investigation to establish whether these neo-connections are reversible, for example by flow restoration or targeting a molecular mediator, could be clinically important.

### Drivers of EndMT in CLI

Arteriolar integrity in ischemic tissue is critically dependant of the attributes of the enveloping SMCs (Frontini et al., 2011; Said et al., 2019; Yin et al., 2015). In this regard, it is noteworthy that arteriolar SMCs in CLI muscles were found to express abundant TGF $\beta$ 1, a growth factor that is associated with ischemic injury (Basilile et al., 1996; Lee et al., 2004; Yamashita et al., 1999). The findings are also consistent with reports linking TGF $\beta$  expression in SMCs with vascular disease, including in PAD (Balint et al., 2019; Ha et al., 2016). The additional *in situ* identification of activated (phosphorylated) SMAD2/3 in the nucleus of endothelial cells of stenotic arterioles is important because it implicates a potentially malicious paracrine signaling axis within ischemic skeletal muscle arterioles. We propose that this SMC-endothelial axis for TGF $\beta$  drives EndMT in arterioles and results in lumen narrowing.

It is also possible that abnormal hemodynamics in the microvasculature could contribute to altering the endothelial phenotype. It is well recognized that physiological shear stress leads to flattening and elongation of endothelial cells (Barbee et al., 1994; Wang et al., 2013), and future studies delineating the impact of ultra-low flow on endothelial cells of the arteriolar tree are warranted. We also cannot exclude the possibility that endothelial cell lumen encroachment could arise, at least in part, from arteriolar vasoconstriction. However, notwithstanding the specific drivers, the arteriolar endothelial remodeling process was sufficiently chronic to result in stable expression of mesenchymal markers and to reconfigure the intercellular adhesion machinery.

### Clinical Implications

The current findings have several potential clinical implications. A sufficient burden of endothelial-cell-based lumen narrowing and closure of small arterioles could limit or abrogate the benefits of operative or percutaneous revascularization of upstream arteries. It is also conceivable that EndMT-associated arteriolar closure is a determinant of the high-risk, but poorly predicted, progression from intermittent claudication to CLI (Annex, 2013). As well, therapies that inhibit EndMT, TGF $\beta$ 1 stimulation, or both in the vasculature of individuals with PAD warrant study (Cooley et al., 2014; Man et al., 2019). Finally, our findings and their clinical implications highlight the need for non-invasive strategies to assess the distal arteriolar bed in patients with advanced PAD.

### Limitations of the Study

The current study was restricted to analyzing muscles harvested from individuals with CLI requiring amputation. This is an important population due to its morbidity, mortality, and utilization of health care

resources (Farber and Eberhardt, 2016; Ma et al., 2014). However, the data cannot be extrapolated to individuals with PAD not requiring amputation and we cannot be sure at what stage of the disease EndMT might be initiated. We also note that the comparator non-PAD group constituted individuals in whom there was no evidence for vascular disease risk factors, whereas most of the CLI subjects had risks, including diabetes and hypertension. The current data cannot ascertain whether any of these risk factors in themselves might predispose to mesenchymal transitioning of microvascular endothelial cells. This important question requires a larger study with appropriate power to detect clinical associations. We note that immersion (versus perfusion) fixation can impact vessel dimensions, although not the observed differences among groups nor the markers of EndMT. Finally, further micro-morphometric studies would be important to determine if arteriolar components outside the endothelial cells, including SMCs and collagen, participate in the arteriolar narrowing/occlusion process that we have identified.

### Conclusion

We have identified a non-atherosclerotic, non-thrombotic form of arteriolar stenosis based on partial endothelial-to-mesenchymal transition. The findings uncover a previously unrecognized microvascular closure process that could underlie the refractory and debilitating ischemic damage of critical limb ischemia.

### Resource Availability

#### Lead Contact

Further information and requests for details regarding resources should be directed to and will be fulfilled by the Lead Contact, J. Geoffrey Pickering ([gpickering@robarts.ca](mailto:gpickering@robarts.ca)).

#### Materials Availability

This study did not generate new unique reagents.

#### Data and Code Availability

The published article includes all data generated and analyzed during this study.

## METHODS

All methods can be found in the accompanying [Transparent Methods supplemental file](#).

## SUPPLEMENTAL INFORMATION

Supplemental Information can be found online at <https://doi.org/10.1016/j.isci.2020.101251>.

## ACKNOWLEDGMENTS

This work was supported by the Canadian Institutes of Health Research (FDN-143326). JGP holds the Heart & Stroke Foundation/Barnett-Ivey Chair.

## AUTHOR CONTRIBUTIONS

Conceptualization, J.G.P.; Methodology J.C. and J.G.P.; Investigation, J.C, H.Y., J-M.A., C.O., Z.N., J. J.L., E.K.P.; Writing—Original Draft, J.C. and J.G.P.; Writing—Reviewing and Editing, J.C., H.Y., and J.G.P.; Funding Acquisition, J.G.P.; Resources, J.C., H.Y., J-M.A., K.J.G., M.H., C.L.R., L.D., A.H.P., and D.L.H.; Supervision, J.G.P, L.D., A.H.P., D.L.H.

## DECLARATION OF INTERESTS

The authors declare no competing interests.

Received: February 6, 2020

Revised: May 3, 2020

Accepted: June 4, 2020

Published: June 26, 2020

## REFERENCES

- Allen, J.D., Miller, E.M., Schwark, E., Robbins, J.L., Duscha, B.D., and Annex, B.H. (2009). Plasma nitrite response and arterial reactivity differentiate vascular health and performance. *Nitric Oxide* 20, 231–237.
- Almasri, J., Adusumalli, J., Asi, N., Lakis, S., Alsawas, M., Prokop, L.J., Bradbury, A., Kolh, P., Conte, M.S., and Murad, M.H. (2019). A systematic review and meta-analysis of revascularization outcomes of infrainguinal chronic limb-threatening ischemia. *J. Vasc. Surg.* 69, 126S–136S.
- Annex, B.H. (2013). Therapeutic angiogenesis for critical limb ischaemia. *Nat. Rev. Cardiol.* 10, 387–396.
- Arpino, J.M., Nong, Z., Li, F., Yin, H., Ghonaim, N., Milkovich, S., Balint, B., O'Neil, C., Fraser, G.M., Goldman, D., et al. (2017). Four-dimensional microvascular analysis reveals that regenerative angiogenesis in ischemic muscle produces a flawed microcirculation. *Circ. Res.* 120, 1453–1465.
- Balint, B., Yin, H., Nong, Z., Arpino, J.M., O'Neil, C., Rogers, S.R., Randhawa, V.K., Fox, S.A., Chevalier, J., Lee, J.J., et al. (2019). Seno-destructive smooth muscle cells in the ascending aorta of patients with bicuspid aortic valve disease. *EBioMedicine* 43, 54–66.
- Barbee, K.A., Davies, P.F., and Lal, R. (1994). Shear stress-induced reorganization of the surface topography of living endothelial cells imaged by atomic force microscopy. *Circ. Res.* 74, 163–171.
- Basile, D.P., Rovak, J.M., Martin, D.R., and Hammerman, M.R. (1996). Increased transforming growth factor-beta 1 expression in regenerating rat renal tubules following ischemic injury. *Am. J. Physiol.* 270, F500–F509.
- Bronner-Fraser, M., Wolf, J.J., and Murray, B.A. (1992). Effects of antibodies against N-cadherin and N-CAM on the cranial neural crest and neural tube. *Dev. Biol.* 153, 291–301.
- Chu, Y.S., Eder, O., Thomas, W.A., Simcha, I., Pincet, F., Ben-Ze'ev, A., Perez, E., Thiery, J.P., and Dufour, S. (2006). Prototypical type I E-cadherin and type II cadherin-7 mediate very distinct adhesiveness through their extracellular domains. *J. Biol. Chem.* 281, 2901–2910.
- Clyne, C.A., Mears, H., Weller, R.O., and O'Donnell, T.F. (1985). Calf muscle adaptation to peripheral vascular disease. *Cardiovasc. Res.* 19, 507–512.
- Coats, P., and Hillier, C. (2000). Differential responses in human subcutaneous and skeletal muscle vascular beds to critical limb ischaemia. *Eur. J. Vasc. Endovasc. Surg.* 19, 387–395.
- Conrad, M.C. (1967). Large and small artery occlusion in diabetics and nondiabetics with severe vascular disease. *Circulation* 36, 83–91.
- Conrad, M.C. (1968). Abnormalities of the digital vasculature as related to ulceration and gangrene. *Circulation* 38, 568–581.
- Cooley, B.C., Nevado, J., Mellad, J., Yang, D., St Hilaire, C., Negro, A., Fang, F., Chen, G., San, H., Walts, A.D., et al. (2014). TGF-beta signaling mediates endothelial-to-mesenchymal transition (EndMT) during vein graft remodeling. *Sci. Transl. Med.* 6, 227ra234.
- Dejana, E., Hirschi, K.K., and Simons, M. (2017). The molecular basis of endothelial cell plasticity. *Nat. Commun.* 8, 14361.
- Evrard, S.M., Lecce, L., Michelis, K.C., Nomura-Kitabayashi, A., Pandey, G., Purushothaman, K.R., d'Escamard, V., Li, J.R., Hadri, L., Fujitani, K., et al. (2016). Endothelial to mesenchymal transition is common in atherosclerotic lesions and is associated with plaque instability. *Nat. Commun.* 7, 11853.
- Farber, A., and Eberhardt, R.T. (2016). The current state of critical limb ischemia: a systematic review. *JAMA Surg.* 151, 1070–1077.
- Feihl, F., Liaudet, L., Levy, B.I., and Waeber, B. (2008). Hypertension and microvascular remodelling. *Cardiovasc. Res.* 78, 274–285.
- Frontini, M.J., Nong, Z., Gros, R., Drangova, M., O'Neil, C., Rahman, M.N., Akawi, O., Yin, H., Ellis, C.G., and Pickering, J.G. (2011). Fibroblast growth factor 9 delivery during angiogenesis produces durable, vasoresponsive microvessels wrapped by smooth muscle cells. *Nat. Biotechnol.* 29, 421–427.
- Gerhardt, H., Wolburg, H., and Redies, C. (2000). N-cadherin mediates pericytic-endothelial interaction during brain angiogenesis in the chicken. *Dev. Dyn.* 218, 472–479.
- Gilbertson-Beadling, S.K., and Fisher, C. (1993). A potential role for N-cadherin in mediating endothelial cell-smooth muscle cell interactions in the rat vasculature. *Lab. Invest.* 69, 203–209.
- Ha, D.M., Carpenter, L.C., Koutakis, P., Swanson, S.A., Zhu, Z., Hanna, M., DeSpiegelaele, H.K., Pipinos, I.I., and Casale, G.P. (2016). Transforming growth factor-beta 1 produced by vascular smooth muscle cells predicts fibrosis in the gastrocnemius of patients with peripheral artery disease. *J. Transl. Med.* 14, 39.
- Hammarsten, J., Bylund-Fellenius, A.C., Holm, J., Schersten, T., and Krotkiewski, M. (1980). Capillary supply and muscle fibre types in patients with intermittent claudication: relationships between morphology and metabolism. *Eur. J. Clin. Invest.* 10, 301–305.
- Hillier, C., Sayers, R.D., Watt, P.A., Naylor, R., Bell, P.R., and Thurston, H. (1999). Altered small artery morphology and reactivity in critical limb ischaemia. *Clin. Sci. (Lond.)* 96, 155–163.
- Ho, T.K., Rajkumar, V., Ponticos, M., Leoni, P., Black, D.C., Abraham, D.J., and Baker, D.M. (2006). Increased endogenous angiogenic response and hypoxia-inducible factor-1alpha in human critical limb ischemia. *J. Vasc. Surg.* 43, 125–133.
- Isakson, B.E., Best, A.K., and Duling, B.R. (2008). Incidence of protein on actin bridges between endothelium and smooth muscle in arterioles demonstrates heterogeneous connexin expression and phosphorylation. *Am. J. Physiol. Heart Circ. Physiol.* 294, H2898–H2904.
- Kovacic, J.C., Dimmeler, S., Harvey, R.P., Finkel, T., Aikawa, E., Krenning, G., and Baker, A.H. (2019). Endothelial to mesenchymal transition in cardiovascular disease: JACC State-of-the-Art Review. *J. Am. Coll. Cardiol.* 73, 190–209.
- Laurent, S., and Boutouyrie, P. (2015). The structural factor of hypertension: large and small artery alterations. *Circ. Res.* 116, 1007–1021.
- Lee, C.W., Stabile, E., Kinnaird, T., Shou, M., Devaney, J.M., Epstein, S.E., and Burnett, M.S. (2004). Temporal patterns of gene expression after acute hindlimb ischemia in mice: insights into the genomic program for collateral vessel development. *J. Am. Coll. Cardiol.* 43, 474–482.
- Ma, V.Y., Chan, L., and Carruthers, K.J. (2014). Incidence, prevalence, costs, and impact on disability of common conditions requiring rehabilitation in the United States: stroke, spinal cord injury, traumatic brain injury, multiple sclerosis, osteoarthritis, rheumatoid arthritis, limb loss, and back pain. *Arch. Phys. Med. Rehabil.* 95, 986–995.e1.
- Man, S., Sanchez Duffhues, G., Ten Dijke, P., and Baker, D. (2019). The therapeutic potential of targeting the endothelial-to-mesenchymal transition. *Angiogenesis* 22, 3–13.
- McGuigan, M.R., Bronks, R., Newton, R.U., Sharman, M.J., Graham, J.C., Cody, D.V., and Kraemer, W.J. (2001). Muscle fiber characteristics in patients with peripheral arterial disease. *Med. Sci. Sports Exerc.* 33, 2016–2021.
- Nagai, N., Ohguchi, H., Nakaki, R., Matsumura, Y., Kanki, Y., Sakai, J., Aburatani, H., and Minami, T. (2018). Downregulation of ERG and FLI1 expression in endothelial cells triggers endothelial-to-mesenchymal transition. *PLoS Genet.* 14, e1007826.
- Narula, N., Dannenberg, A.J., Olin, J.W., Bhatt, D.L., Johnson, K.W., Nadkarni, G., Min, J., Torii, S., Poojary, P., Anand, S.S., et al. (2018). Pathology of peripheral artery disease in patients with critical limb ischemia. *J. Am. Coll. Cardiol.* 72, 2152–2163.
- Navarro, P., Ruco, L., and Dejana, E. (1998). Differential localization of VE- and N-cadherins in human endothelial cells: VE-cadherin competes with N-cadherin for junctional localization. *J. Cell Biol.* 140, 1475–1484.
- Norgren, L., Hiatt, W.R., Dormandy, J.A., Nehler, M.R., Harris, K.A., and Fowkes, F.G. (2007). Inter-society consensus for the management of peripheral arterial disease (TASC II). *J. Vasc. Surg.* 45 (Suppl S), S5–S67.
- Park, J.B., and Schiffrin, E.L. (2001). Small artery remodeling is the most prevalent (earliest?) form of target organ damage in mild essential hypertension. *J. Hypertens.* 19, 921–930.
- Robbins, J.L., Jones, W.S., Duscha, B.D., Allen, J.D., Kraus, W.E., Regensteiner, J.G., Hiatt, W.R., and Annex, B.H. (2011). Relationship between leg muscle capillary density and peak hyperemic blood flow with endurance capacity in peripheral artery disease. *J. Appl. Physiol.* (1985) 111, 81–86.
- Rouso, D.L., Pearson, C.A., Gaber, Z.B., Miquelajauregui, A., Li, S., Portera-Cailliau, C.,

Morrissey, E.E., and Novitch, B.G. (2012). Foxp-mediated suppression of N-cadherin regulates neuroepithelial character and progenitor maintenance in the CNS. *Neuron* 74, 314–330.

Said, S.S., Yin, H., Elfarnawany, M., Nong, Z., O’Neil, C., Leong, H., Lacefield, J.C., Mequanint, K., and Pickering, J.G. (2019). Fortifying angiogenesis in ischemic muscle with FGF9-loaded electrospun poly(ester amide) fibers. *Adv. Healthc. Mater.* 8, e1801294.

Salomon, D., Ayalon, O., Patel-King, R., Hynes, R.O., and Geiger, B. (1992). Extrajunctional distribution of N-cadherin in cultured human endothelial cells. *J. Cell Sci.* 102 (Pt 1), 7–17.

Sanchez-Duffhues, G., Orlova, V., and Ten Dijke, P. (2016). In brief: endothelial-to-mesenchymal transition. *J. Pathol.* 238, 378–380.

Saygin, D., Highland, K.B., and Tonelli, A.R. (2019). Microvascular involvement in systemic sclerosis and systemic lupus erythematosus. *Microcirculation* 26, e12440.

Shishehbor, M.H., White, C.J., Gray, B.H., Menard, M.T., Lookstein, R., Rosenfield, K., and Jaff, M.R. (2016). Critical limb ischemia: an expert statement. *J. Am. Coll. Cardiol.* 68, 2002–2015.

Springer, J., and Villa-Forte, A. (2013). Thrombosis in vasculitis. *Curr. Opin. Rheumatol.* 25, 19–25.

Tsui, J.C., Baker, D.M., Biecker, E., Shaw, S., and Dashwood, M.R. (2002). Potential role of endothelin 1 in ischaemia-induced angiogenesis in critical leg ischaemia. *Br. J. Surg.* 89, 741–747.

Vafaie, F., Yin, H., O’Neil, C., Nong, Z., Watson, A., Arpino, J.M., Chu, M.W., Holdsworth, D.W., Gros, R., and Pickering, J.G. (2014). Collagenase-resistant collagen promotes mouse aging and vascular cell senescence. *Aging Cell* 13, 121–130.

Wang, C., Baker, B.M., Chen, C.S., and Schwartz, M.A. (2013). Endothelial cell sensing of flow direction. *Arterioscler. Thromb. Vasc. Biol.* 33, 2130–2136.

Welch-Reardon, K.M., Wu, N., and Hughes, C.C. (2015). A role for partial endothelial-

mesenchymal transitions in angiogenesis? *Arterioscler. Thromb. Vasc. Biol.* 35, 303–308.

Wheelock, M.J., Shintani, Y., Maeda, M., Fukumoto, Y., and Johnson, K.R. (2008). Cadherin switching. *J. Cell Sci.* 121, 727–735.

Whittaker, P., Kloner, R.A., Boughner, D.R., and Pickering, J.G. (1994). Quantitative assessment of myocardial collagen with picrosirius red staining and circularly polarized light. *Basic Res. Cardiol.* 89, 397–410.

Yamashita, K., Gerken, U., Vogel, P., Hossmann, K., and Wiessner, C. (1999). Biphasic expression of TGF-beta1 mRNA in the rat brain following permanent occlusion of the middle cerebral artery. *Brain Res.* 836, 139–145.

Yin, H., Frontini, M.J., Arpino, J.M., Nong, Z., O’Neil, C., Xu, Y., Balint, B., Ward, A.D., Chakrabarti, S., Ellis, C.G., et al. (2015). Fibroblast growth factor 9 imparts hierarchy and vasoreactivity to the microcirculation of renal tumors and suppresses metastases. *J. Biol. Chem.* 290, 22127–22142.

**Supplemental Information**

**Obstruction of Small Arterioles in Patients  
with Critical Limb Ischemia due to Partial  
Endothelial-to-Mesenchymal Transition**

**Jacqueline Chevalier, Hao Yin, John-Michael Arpino, Caroline O'Neil, Zengxuan Nong, Kevin J. Gilmore, Jason J. Lee, Emma Prescott, Matthew Hewak, Charles L. Rice, Luc Dubois, Adam H. Power, Douglas W. Hamilton, and J. Geoffrey Pickering**

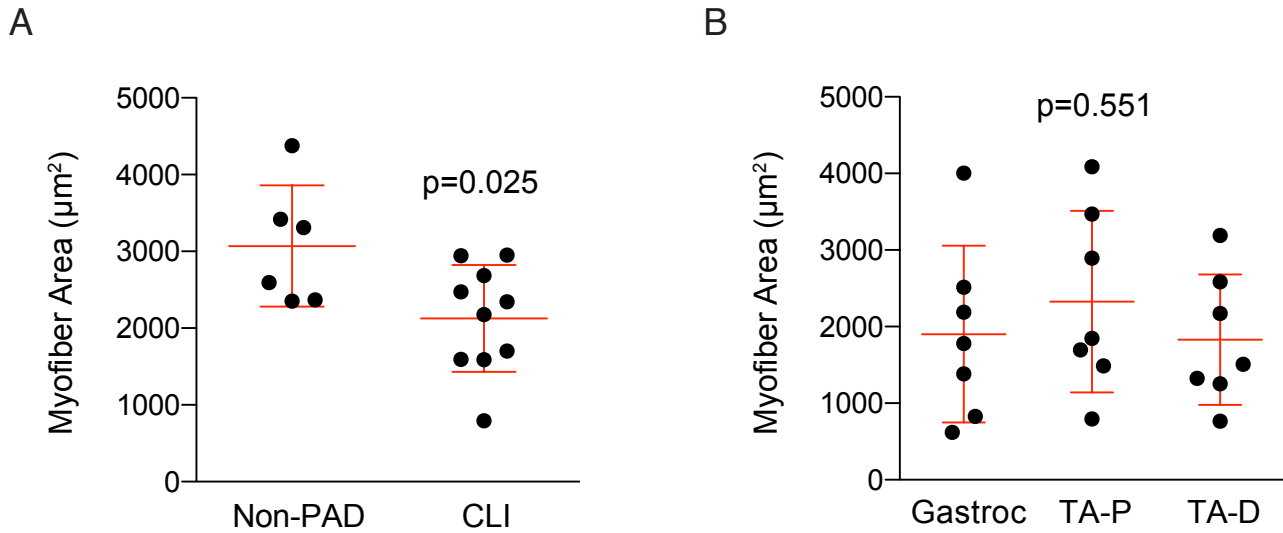
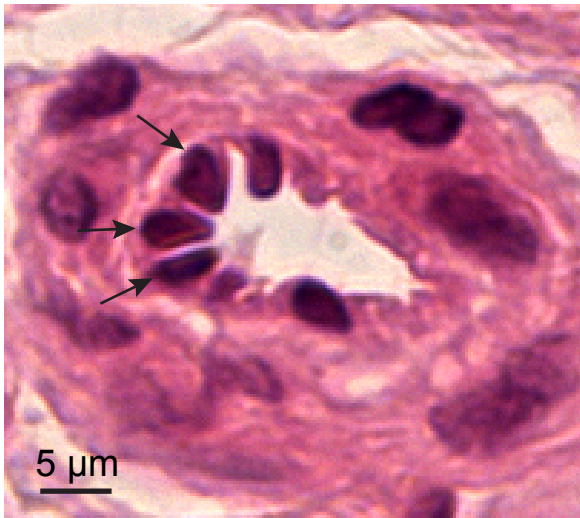


**Figure S1 Myofiber area in skeletal muscles harvested from subjects with critical limb ischemia**  
*Related to Figure 1*

**A.** Graph depicting the mean myofiber area in lower limb skeletal muscles from individuals without peripheral artery disease (non-PAD) and in patients with critical limb ischemia (CLI). **B.** Graph showing mean myofiber area in three different skeletal muscle territories from individuals with critical limb ischemia. Data are presented on a per patient basis, as mean and standard deviation. Gastroc, gastrocnemius; TA-P, tibialis anterior proximal; TA-D, tibialis anterior distal.

A



B

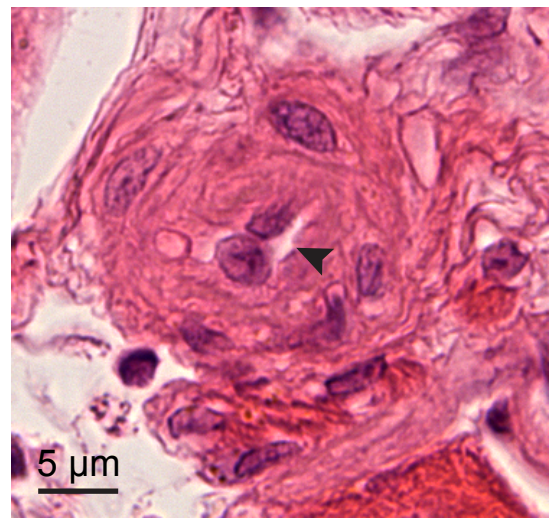


**Figure S2 Narrowed intramuscular arterioles in CLI muscles** *Related to Figure 3*

A, B. Light micrographs of hematoxylin and eosin-stained arterioles within the tibialis anterior muscles from two individuals with CLI. The image in A, shows luminal encroachment by bulky, re-oriented pyramidal-shaped endothelial cells with enlarged nuclei (arrows). The image in B shows a high-grade narrowing of a small arteriole with only a slit-like lumen (arrowhead). In both instances, there is no evidence for fresh or chronic thrombus in the lumen.

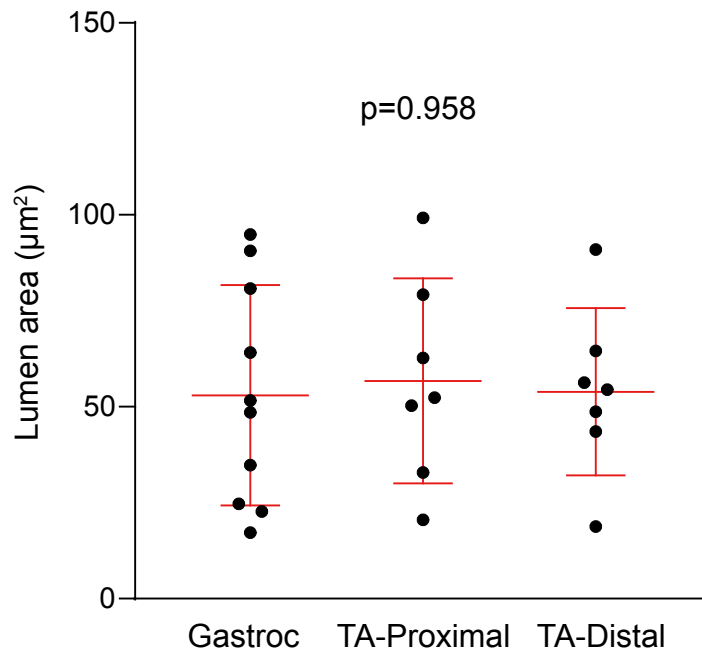


**Figure S3 Arteriolar lumen area in different skeletal muscles harvested from subjects with critical limb ischemia** *Related to Figure 3*

Graph showing mean lumen area for small arterioles (those with an outer endothelial circumference  $\leq 60 \mu\text{m}$ ) in three different skeletal muscle territories from individuals with critical limb ischemia. Data are presented on a per patient basis, as mean and standard deviation.

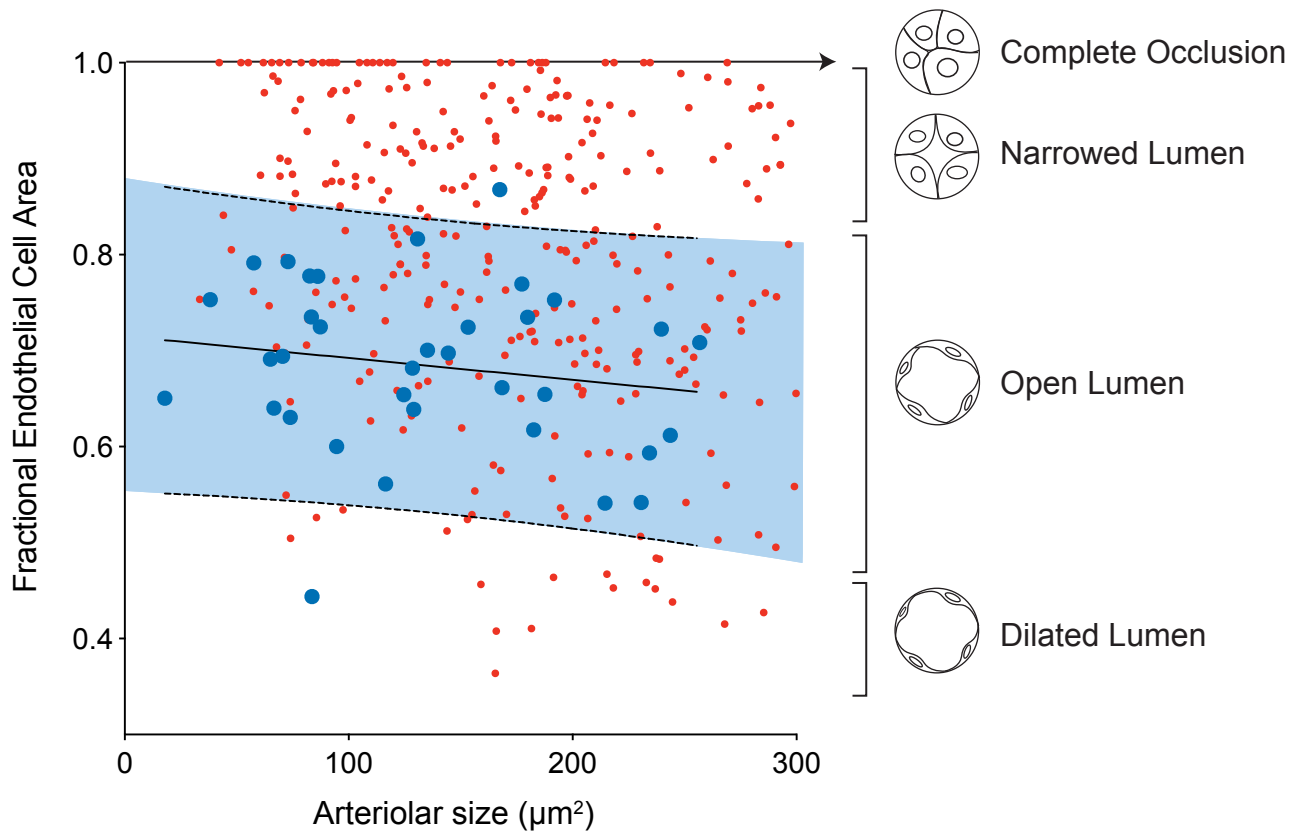


**Figure S4 Luminal encroachment by endothelial cells in small skeletal muscle arterioles** *Related to Figure 3*

Graph of the fractional endothelial cell area (endothelial area divided by the total area bounded by the outer endothelial border) vs. arteriolar size (area bounded by the outer endothelial border) for small skeletal muscle arterioles. Arteriolar measurements from non-peripheral artery disease muscles are depicted in blue and the 90% prediction band is shaded blue. Arteriolar measurements from critical limb ischemia muscles are depicted in red. 42% of all critical limb ischemia arterioles have a fractional endothelial area above the 90% prediction band - 33% are narrowed and 9% are fully occluded. Schematic representations of corresponding arteriolar morphologies are shown on the right. Arterioles above the prediction band have bulky endothelial cells that narrow the lumen and may completely occlude it. For the latter, the fractional endothelial cell area is 1.0.

**Table S1 Subject Demographics** *Related to Figures 1-6*

Subject	Sex	Age	Diabetes	Smoking	Prior Revascularization Procedure*	Hypertension	Muscles Harvested
<b>CLI Subjects</b>							
1	M	60	N	Y	Y	Y	Gastrocnemius
2	F	31	T1	Y	Y	N	Gastrocnemius
3	M	57	T1	Y	N	Y	Gastrocnemius Tibialis Anterior Proximal Tibialis Anterior Distal
4	M	72	T2	Y	N	Y	Gastrocnemius
5	F	79	N	N	Y	Y	Gastrocnemius Tibialis Anterior Proximal Tibialis Anterior Distal
6	F	68	T2	Y	N	Y	Gastrocnemius Tibialis Anterior Proximal Tibialis Anterior Distal
7	M	90	T2	Y	N	N	Gastrocnemius Tibialis Anterior Proximal Tibialis Anterior Distal
8	F	74	T2	Y	Y	Y	Gastrocnemius Tibialis Anterior Proximal Tibialis Anterior Distal
9	F	67	T2	N	Y	Y	Gastrocnemius Tibialis Anterior Proximal Tibialis Anterior Distal
10	F	50	T2	Y	N	N	Gastrocnemius Tibialis Anterior Proximal Tibialis Anterior Distal
<b>Non-PAD Subjects</b>							
1	M	50	N	N	N/A	n.d.	Tibialis Anterior
2	F	18	N	N	N/A	n.d.	Tibialis Anterior
3	F	61	N	n.d.	N/A	n.d.	Vastus Lateralis
4	M	57	N	n.d.	N/A	n.d.	Vastus Lateralis
5	F	62	N	n.d.	N/A	n.d.	Vastus Lateralis
6	F	61	N	n.d.	N/A	n.d.	Vastus Lateralis

\*of the subsequently amputated limb

N, No diabetes or hypertension; T1, Type 1 diabetes; T2, Type 2 diabetes; n.d., not determined; N/A not applicable

**Table S2 Histopathology of Skeletal Muscle in Amputation Specimens** *Related to Figure 1*

Subject	Muscle	Myofiber Atrophy	Necrosis	Central Nuclei	Inflammation	Fibrosis
1	Gastrocnemius	+	-	Y	1	2
2	Gastrocnemius	++	++	Y	3	3
3	Gastrocnemius	+	-	N	0	0
	Tibialis Anterior Proximal	++	++	N	1	1
	Tibialis Anterior Distal	++	+	Y	1	0
4	Gastrocnemius	+	-	N	0	0
5	Gastrocnemius	++	+	Y	2	0
	Tibialis Anterior Proximal	++	+	Y	1	0
	Tibialis Anterior Distal	+	+	Y	2	1
6	Gastrocnemius	++	++	N	2	2
	Tibialis Anterior Proximal	+	-	N	1	1
	Tibialis Anterior Distal	++	+	N	2	0
7	Gastrocnemius	++	++	Y	2	2
	Tibialis Anterior Proximal	++	++	Y	1	1
	Tibialis Anterior Distal	++	++	Y	2	2
8	Gastrocnemius	+	-	N	0	0
	Tibialis Anterior Proximal	++	++	Y	1	1
	Tibialis Anterior Distal	+	-	N	0	1
9	Gastrocnemius	++	+	Y	0	0
	Tibialis Anterior Proximal	++	+	Y	1	0
	Tibialis Anterior Distal	+	+	Y	1	0
10	Gastrocnemius	+++	+++	Y	3	3
	Tibialis Anterior Proximal	+++	+++	Y	3	3
	Tibialis Anterior Distal	+++	+++	Y	3	3

Myofiber atrophy and necrosis: -, none seen; +, < 30% of myofibers; ++, 30-60% of myofibers; +++, > 60% of myofibers

Y, yes; N, no

Inflammation and fibrosis: 0, none; 1, mild; 2, moderate; 3, severe

**Table S1 Subject Demographics** *Related to Figures 1-6*

Subject	Sex	Age	Diabetes	Smoking	Prior Revascularization Procedure*	Hypertension	Muscles Harvested
<b>CLI Subjects</b>							
1	M	60	N	Y	Y	Y	Gastrocnemius
2	F	31	T1	Y	Y	N	Gastrocnemius
3	M	57	T1	Y	N	Y	Gastrocnemius Tibialis Anterior Proximal Tibialis Anterior Distal
4	M	72	T2	Y	N	Y	Gastrocnemius
5	F	79	N	N	Y	Y	Gastrocnemius Tibialis Anterior Proximal Tibialis Anterior Distal
6	F	68	T2	Y	N	Y	Gastrocnemius Tibialis Anterior Proximal Tibialis Anterior Distal
7	M	90	T2	Y	N	N	Gastrocnemius Tibialis Anterior Proximal Tibialis Anterior Distal
8	F	74	T2	Y	Y	Y	Gastrocnemius Tibialis Anterior Proximal Tibialis Anterior Distal
9	F	67	T2	N	Y	Y	Gastrocnemius Tibialis Anterior Proximal Tibialis Anterior Distal
10	F	50	T2	Y	N	N	Gastrocnemius Tibialis Anterior Proximal Tibialis Anterior Distal
<b>Non-PAD Subjects</b>							
1	M	50	N	N	N/A	n.d.	Tibialis Anterior
2	F	18	N	N	N/A	n.d.	Tibialis Anterior
3	F	61	N	n.d.	N/A	n.d.	Vastus Lateralis
4	M	57	N	n.d.	N/A	n.d.	Vastus Lateralis
5	F	62	N	n.d.	N/A	n.d.	Vastus Lateralis
6	F	61	N	n.d.	N/A	n.d.	Vastus Lateralis

\*of the subsequently amputated limb

N, No diabetes or hypertension; T1, Type 1 diabetes; T2, Type 2 diabetes; n.d., not determined; N/A not applicable

**Table S2 Histopathology of Skeletal Muscle in Amputation Specimens** *Related to Figure 1*

Subject	Muscle	Myofiber Atrophy	Necrosis	Central Nuclei	Inflammation	Fibrosis
1	Gastrocnemius	+	-	Y	1	2
2	Gastrocnemius	++	++	Y	3	3
3	Gastrocnemius	+	-	N	0	0
	Tibialis Anterior Proximal	++	++	N	1	1
	Tibialis Anterior Distal	++	+	Y	1	0
4	Gastrocnemius	+	-	N	0	0
5	Gastrocnemius	++	+	Y	2	0
	Tibialis Anterior Proximal	++	+	Y	1	0
	Tibialis Anterior Distal	+	+	Y	2	1
6	Gastrocnemius	++	++	N	2	2
	Tibialis Anterior Proximal	+	-	N	1	1
	Tibialis Anterior Distal	++	+	N	2	0
7	Gastrocnemius	++	++	Y	2	2
	Tibialis Anterior Proximal	++	++	Y	1	1
	Tibialis Anterior Distal	++	++	Y	2	2
8	Gastrocnemius	+	-	N	0	0
	Tibialis Anterior Proximal	++	++	Y	1	1
	Tibialis Anterior Distal	+	-	N	0	1
9	Gastrocnemius	++	+	Y	0	0
	Tibialis Anterior Proximal	++	+	Y	1	0
	Tibialis Anterior Distal	+	+	Y	1	0
10	Gastrocnemius	+++	+++	Y	3	3
	Tibialis Anterior Proximal	+++	+++	Y	3	3
	Tibialis Anterior Distal	+++	+++	Y	3	3

Myofiber atrophy and necrosis: -, none seen; +, < 30% of myofibers; ++, 30-60% of myofibers; +++, > 60% of myofibers

Y, yes; N, no

Inflammation and fibrosis: 0, none; 1, mild; 2, moderate; 3, severe

## TRANSPARENT METHODS

### METHODS DETAILS

#### Resources

The source and identifiers of all antibodies, chemicals, and software used are listed in the Key Resources table, below.

#### Specimen Collection

All human tissue samples and patient information were collected with written, informed consent from patients using protocols approved by the Western University Review Board for Health Sciences Research Involving Human Subjects and in accordance with the 1964 Declaration of Helsinki. Skeletal muscle specimens were collected from 10 consecutive consenting individuals (6 female, 4 male) with CLI, immediately following below-knee (n=9) or above-knee (n=1) amputation. Skeletal muscle specimens 1 cm x 1 cm x 0.5 cm in size were harvested from the proximal tibialis anterior muscle, distal tibialis anterior muscle, and/or the gastrocnemius muscle of all individuals with CLI (n=24 samples). Non-PAD muscle specimens were collected from 6 individuals (4 female, 2 male) with no peripheral artery or skeletal muscle disease. Samples were from the tibialis anterior muscle (n=2 Amsbio) or vastus lateralis muscle (n=4), the latter retrieved by needle-biopsy within 24 hours of death.

#### Histologic Analysis of Skeletal Muscle Pathology

Skeletal muscle samples were immersion-fixed in 10% formalin, embedded in paraffin, and 5- $\mu$ m-thick cross-sections were stained with hematoxylin and eosin, Mason's trichrome, or picrosirius red (Polysciences, Warrington, PA, USA). Full sections were digitally scanned (Leica Aperio AT2 bright field scanner) and evaluated using Aperio ImageScope slide viewing software (Leica Biosystems). The extent of myofiber atrophy, defined as shrunken myofibers with either abnormally rounded or sharply angular cross-sectional borders, was graded based on occupying <30%, 30-60%, or >60% of the tissue section area. Myofiber cross-sectional area was also quantified from 80-100 myofibers per patient, measure from

all myofibers transected by randomly placed parallel lines on 12-20 images per patient. Myocyte necrosis was determined based on pale eosin staining and a waxy appearance of myofibers, with or without mononuclear cell infiltration (Zenker's degeneration) (Arpino et al., 2017; Wells, 1909). Necrosis was semi-quantified as for myofiber atrophy. Interstitial inflammation and fibrosis were each ranked on a severity scale of 0–3. Fibrosis was assessed from the blue colorization in Mason's trichrome-stained sections and from birefringence assessment using circular polarization microscopy (Nong et al., 2011; Said et al., 2019; Vafaie et al., 2014; Whittaker et al., 1994). For the latter, picrosirius-red-stained sections were imaged using an Olympus BX51 microscope with BX series circular polarizer/interference filters, a liquid crystal compensator and a CCD camera, and birefringence signals visualized using Abrio imaging software (Cambridge Research & Instrumentation, Woburn, MA, USA).

## **Immunostaining**

Immunofluorescence staining was undertaken following antigen retrieval (10 mM sodium citrate buffer, pH 6.0, pressure-heater for 30 minutes) using methods as described (Balint et al., 2019; Rocnik et al., 2001) and antibodies listed in the Key Resources table below. Endothelial cells were identified using one of two anti-CD31 antibodies, selected to enable double and triple immuno-labeling. SMCs were similarly detected using one of two anti-smooth muscle (SM)  $\alpha$ -actin antibodies. The optimized antibody combinations for multi-labeling are delineated in the Multiplex Immunostaining Details table below. Nuclei were visualized with 4',6-diamidino-2-phenylindole (DAPI) Fluoromount-G (SouthernBiotech, 0100-020). Images were captured for data analysis using: 1) an Olympus BX-51 microscope with RETIGA EXi Mono 12-bit camera (QImaging) and Northern Eclipse software (EMPIX Imaging Inc.); 2) a Carl Zeiss Imager M2m microscope with AxioCam HRm camera and AxioVision (Zeiss) software; 3) a Leica Aperio VERSA Fluorescence Pathology Scanner, using a 40x objective, a z-stack range 1.2  $\mu$ m, and step size of 0.2  $\mu$ m; or 4) a Nikon A1 hybrid laser-scanning confocal microscope (Galvano scanning, lasers 405, 488, 561, and 640 nm excitation wavelengths, as appropriate) with NIS Elements software, including for 3D reconstructions and video generation.

### **Analysis of Capillary and Arteriole Density**

Capillary content was assessed based on quantifying CD31-positive microvessels of lumen diameter  $<8 \mu\text{m}$ . Arteriole content was determined from intramuscular arterioles, 8-60  $\mu\text{m}$  in diameter, that co-immunolabeled for CD31 and smooth muscle (SM)  $\alpha$ -actin. Densities were determined in 5-10 equally spaced fields of view (60x objective) imaged with an Olympus BX-51 microscope and quantified using ImageJ (NIH).

### **Analysis of Arteriolar Morphometry**

Arteriole morphology was quantified from sections imaged by widefield microscopy (Carl Zeiss Imager M2m microscope) with AxioVision (Zeiss) Software. Lumen area, defined as the area within the inner endothelial cell border, was measured from all cross-sectioned arterioles from 8-15 equally spaced fields of view (40x objective) using ImageJ. Arteriolar size, defined as the circumference at the outer endothelial cell border, was similarly determined. Fractional endothelial cell area was determined as the endothelial cell area divided by the area bound by the outer endothelial cell border. Endothelial cell nuclear aspect ratio was assessed in DAPI-stained tissues based on the linear measurements tangential and orthogonal to the vessel border, using ImageJ.

### **Assessment of N-cadherin, EndMT markers, and TGF $\beta$ signaling in arterioles**

Expression of N-cadherin in endothelial cells was assessed by double-immunolabeling for CD31 and N-cadherin (see Multiplex Immunostaining Details). Samples were imaged with Carl Zeiss Imager M2m microscope ensuring consistent image capture parameters based on recorded acquisition settings and reference slides. The mean intensity of the N-cadherin signal in the endothelium was measured in all arterioles in 10-15 equally spaced fields of view (40x objective) using ImageJ.

Endothelial cell expression of S100A4, SNAIL1, and pSMAD2/3 were assessed by double immunostaining for the respective target and CD31. The percentage of arterioles containing endothelial cells expressing the target protein was assessed in digitally scanned sections of  $\sim 25 \text{ mm}^2$  of skeletal muscle (Leica Aperio VERSA) and determined from a mean of 35 randomly selected arterioles per tissue sample.

Expression of TGF $\beta$ 1 was assessed by immunostaining using antibodies depicted in the Key Resources and Multiplex Immunostaining Details tables, below. Sections were digitally scanned (Leica Aperio VERSA) under identical exposure and dynamic range conditions. The mean pixel intensity and event area was measured in 25 randomly selected arterioles per sample using the Aperio Area Quantification FL Algorithm, yielding an integrated density (product of the mean pixel intensity and event area for each vessel) for the TGF $\beta$ 1 signal. The integrated density was averaged for each subject.

### **Statistical Analysis**

The distributions of myofiber diameters, microvascular densities, arteriolar morphometry measurements, the prevalence of arterioles immuno-positive for a given protein, and endothelial cell protein signal intensities were assessed for normality using D'Agostino and Pearson omnibus normality test. Non-normally distributed data are presented as median and interquartile range (IQR). Comparisons between two groups were evaluated by Mann-Whitney test (for non-paired data) or Wilcoxon matched-pairs test (for paired data). For multiple comparisons, specifically among vessel caliber-specific lumen areas, the p value was corrected using the Benjamini-Hochberg procedure. Normally distributed data are reported as mean  $\pm$  standard deviation, and group comparisons made by t-test or, in the case of myofiber diameter in different muscle zones, by repeated measures analysis of variance. To define an upper limit of normal for the fractional endothelial cell area and account for different arteriolar calibers, the fractional endothelial cell area was plotted against arteriolar size (the area bound by the outer endothelial cell border) in 45 non-PAD arterioles with an outer endothelial cell circumference of 20-60  $\mu$ m, and the 90% prediction band determined (GraphPad Prism 8).

## Key Resources

REAGENT	SOURCE	IDENTIFIER
Antibodies		
Rabbit anti-CD31 (a) 1:50	Thermo Fisher Scientific	RB-10333-P1
Mouse anti-CD31 (b) 1:20	Agilent	M0823
Mouse anti-SM $\alpha$ -actin (a) 1:100	Agilent	M0851
Goat anti-SM $\alpha$ -actin (b) 1:100	Novus Biologicals	NB300-978
Rabbit anti-N-Cadherin 1:400	Novus Biologicals	NB200-592
Rabbit anti-S100A4 1:100	Abcam	ab41532
Mouse anti-SNAIL1 1:50	Thermo Fisher Scientific	14-9859-82
Rabbit anti-TGF $\beta$ 1 1:100	Abcam	ab92486
Rabbit anti-phospho-SMAD2/3 1:100	Cell Signaling Technology	3108
Biotinylated donkey anti-mouse IgG 1:100	Jackson ImmunoResearch	715-005-151
Biotinylated goat anti-mouse IgG 1:100	Jackson ImmunoResearch	115-005-166
Biotinylated goat anti-rabbit IgG 1:100	Jackson ImmunoResearch	111-065-144
DyLight 649-conjugated streptavidin 1:200	Vector Laboratories	SA-5649
Alexa Fluor 488- conjugated goat anti-rabbit IgG 1:200	Thermo Fisher Scientific	A11008
Alexa Fluor 546-conjugated goat anti-mouse IgG 1:200	Thermo Fisher Scientific	A11003
Alexa Fluor 488-conjugated donkey anti-goat IgG 1:200	Thermo Fisher Scientific	A11055
Alexa Fluor 546-conjugated donkey anti-rabbit IgG 1:200	Thermo Fisher Scientific	A10040
Alexa Fluor 647-conjugated donkey anti-mouse IgG 1:200	Thermo Fisher Scientific	A31571

Chemicals		
Formalin	Fisher Scientific	SF98-20
Harris Hematoxylin	Leica Biosystems	3801561
Eosin	Leica Biosystems	3801601
DAPI Fluoromount-G	SouthernBiotech	0100-020
Software and Algorithms		
ImageJ	National Institute of Health	
NIS Elements	Nikon Instruments	
Aperio ImageScope	Leica Biosystems	
GraphPad Prism 8	GraphPad Software	

## Multiplex Immunostaining Details

### Pair 1: CD31 and SM $\alpha$ -actin

Primary Antibody	Secondary Antibody
CD31 (a): Rabbit polyclonal	Alexa Fluor 488- conjugated goat anti-rabbit IgG
SM $\alpha$ -actin (a): Mouse monoclonal	Alexa Fluor 546-conjugated goat anti-mouse IgG

### Pair 2: CD31 and N-cadherin

Primary Antibody	Secondary Antibody
CD31 (b): Mouse monoclonal	biotinylated goat anti-mouse IgG DyLight 649-conjugated streptavidin
N-Cadherin: Rabbit polyclonal	Alexa Fluor 488- conjugated goat anti-rabbit IgG

### Pair 3: CD31 and S100A4

Primary Antibody	Secondary Antibody
CD31 (b): Mouse monoclonal anti-CD31	biotinylated goat anti-mouse IgG DyLight 649-conjugated streptavidin
S100A4: Rabbit polyclonal	Alexa Fluor 488- conjugated goat anti-rabbit IgG

**Pair 4: CD31 and SNAIL1**

Primary Antibody	Secondary Antibody
CD31 (a): Rabbit polyclonal	Alexa Fluor 488- conjugated goat anti-rabbit IgG
SNAIL1: Mouse monoclonal	biotinylated goat anti-mouse IgG DyLight 649-conjugated streptavidin

**Pair 5: CD31 and pSMAD2**

Primary Antibody	Secondary Antibody
CD31 (b): Mouse monoclonal	biotinylated goat anti-mouse IgG DyLight 649-conjugated streptavidin
Phospho-Smad2/3: Rabbit polyclonal	Alexa Fluor 488- conjugated goat anti-rabbit IgG

**Triplet 1: CD31, SM- $\alpha$ -actin and TGF $\beta$ 1**

Primary Antibody	Secondary Antibody
CD31 (b): Mouse monoclonal	biotinylated goat anti-mouse IgG DyLight 649-conjugated streptavidin
SM $\alpha$ -actin (b): Goat polyclonal	Alexa Fluor 488-conjugated donkey anti-goat IgG
TGF $\beta$ 1: Rabbit polyclonal	Alexa Fluor 546-conjugated donkey anti-rabbit IgG

**SUPPLEMENTAL REFERENCES**

Nong, Z., O'Neil, C., Lei, M., Gros, R., Watson, A., Rizkalla, A., Mequanint, K., Li, S., Frontini, M.J., Feng, Q., *et al.* (2011). Type I collagen cleavage is essential for effective fibrotic repair after myocardial infarction. *Am J Pathol* 179, 2189-2198.

Rocnik, E., Seward, L., and Pickering, J.G. (2001). HSP47 expression by smooth muscle cells is increased during arterial development and lesion formation and is inhibited by fibrillar collagen. *Arterioscler Thromb Vasc Biol* 21, 40-46.

Wells, H.G. (1909). The pathogenesis of waxy degeneration of striated muscles (Zenker's degeneration). *J Exp Med* 11, 1-9.